Remote and in situ observations of an unusual Earth-directed Coronal Mass Ejection from multiple viewpoints

T. Nieves-Chinchilla[1], R. Colaninno[2], A. Vourlidas[2], A. Szabo[3],

R.P.Lepping[3], S.A.Boardsen[4], B.J. Anderson[5], and H. Korth[5]

T. Nieves-Chinchilla, CUA, Teresa.Nieves@nasa.gov

[1] Catholic University of America,

Washington, DC, USA.

[2] Space Sciences Division, Naval Research

Laboratory, Washington, DC, USA.

[3] Heliospheric Physic Laboratory, NASA

Goddard Space Flight Center, Greenbelt,

USA

[4] Heliophysics Science Division, NASA

Goddard Space Flight Center, Greenbelt,

USA

[5] The Johns Hopkins University Applied

Physics Laboratory, Laurel, MD, USA.

Abstract.

During June 16-21, 2010, an Earth-directed Coronal Mass Ejection (CME) event was observed by instruments onboard STEREO, SOHO, MESSENGER and Wind. This event was the first direct detection of a rotating CME in the middle and outer corona. Here, we carry out a comprehensive analysis of the evolution of the CME in the interplanetary medium comparing in-situ and remote observations, with analytical models and three-dimensional reconstructions. In particular, we investigate the parallel and perpendicular cross section expansion of the CME from the corona through the heliosphere up to 1 AU. We use height-time measurements and the Gradual Cylindrical Shell (GCS) technique to model the imaging observations, remove the projection effects, and derive the 3-dimensional extent of the event. Then, we compare the results with in-situ analytical Magnetic Cloud (MC) models, and with geometrical predictions from past works. We find that the parallel (along the propagation plane) cross section expansion agrees well with the in-situ model and with the Bothmer & Schwenn [1998] empirical relationship based on in-situ observations between 0.3 and 1 AU. Our results effectively extend this empirical relationship to about 5 solar radii. The expansion of the perpendicular diameter agrees very well with the in-situ results at MESSENGER (~ 0.5 AU) but not at 1 AU. We also find a slightly different, from Bothmer & Schwenn [1998], empirical relationship for the perpendicular expansion. More importantly, we find no evidence that the CME undergoes a significant latitudinal over-expansion as it is commonly assumed.

Instead, we find evidence that effects due to CME rotation and expansion can be easily confused in the images leading to a severe overestimation of the proper 3D size of the event. Finally, we find that the reconstructions of the CME morphology from the in-situ observations at 1 AU are in agreement with the remote sensing observations but they show a big discrepancy at MESSENGER. We attribute this discrepancy to the ambiguity of selecting the proper boundaries due to the lack of accompanying plasma measurements.

1. Introduction

The heliospheric counterparts of Coronal Mass Ejections (CMEs), usually studied with in-situ instrumentation, are referred as Interplanetary CMEs (ICMEs). The study of the initiation, propagation and evolution of ICMEs is of special interest, since they are the primary cause of geo-effective space weather events. Knowledge of the magnetic structure of CMEs in the interplanetary medium is crucial to connect the CME origins on the Sun to their effects on the Earth [Hidalgo et al., 2011].

In-situ measurements suggest that a third of ICMEs observed have a magnetic flux rope structure known as a Magnetic Cloud (MC) [Gosling et al., 1990]. The in-situ features of MCs include an elevation in the magnetic field magnitude, rotation in at least one component of the magnetic field, and low proton-β plasma parameter [Burlaga et al., 1981]. Naturally, ICME studies are usually focused on those events that contain MCs. There are two main reasons: one, because of their relatively well-defined magnetic topology, and, two, because MCs drive the biggest geomagnetic storms (e.g., Richardson et al. [2002]).

Many of the models developed for MCs are based on the concept of a flux-rope in a force-free configuration (Burlaga [1988], Lepping et al. [1990]). These models take into consideration only a subset of the characteristics of MCs as defined by Burlaga et al. [1981]. Other models relax the force-free condition [Owens, 2006] and attempt to describe MCs in their full context with a minimum set of assumptions. Or instead, models as that of Hidalgo & Nieves-Chinchilla [2012] represent an analytical approach to the global magnetic field topology of MCs focussing in the understanding of the physical mechanism

inside the whole structure. However, it is fair to say that they all describe a limited subset of the properties of MCs.

A relatively recent technique, based on solving the Grad-Shafranov equation inside MCs [Hu & Sonnerup, 2002] enables to reconstruct the MC cross section, under a different set of assumptions, and provides a new understanding of these interplanetary events. Such results show that MCs are far from being circular [Möstl et al., 2008].

In all cases, the modeling of in-situ observations of MCs is based on a one-dimensional set of measurements made only along a line cutting through the structure. These measurements are clearly insufficient to describe the evolution of the structure since ICMEs may undergo significant changes from the inner corona and, even, during they pass over an observing spacecraft.

Using Helios data, Bothmer & Schwenn [1998] carried out a MC survey at different solar distances (from 0.3 AU to 1 AU). Assuming a circular cross-section, they derived the rate of expansion for the cross-section

$$Diameter = a(x)^n \qquad with \quad n = 0.78 \tag{1}$$

where x is the heliocentric distance, and a is a constant. This rate of cross-section expansion implies that the density decreases proportionally as $x^{-2.4}$ which in turn implies that plasma pressure is more important in the initial stages of the ICME than at 1 AU, and should be taken into account in the ICME expansion.

Magnetohydrodynamic (MHD) 3D simulations predict a distortion of the MC cross-section, known as 'pancaking', with the thinning taking place in the propagation direction [Riley & Crooker, 2004; Riley et al., 2004]. This distortion is sometimes observed in the remote sensing data for ideal CME-spacecraft configuration.

From the point of view of the in-situ observations, an asymmetric profile in the magnetic field magnitude is thought to be a consequence of this flattening of the ICME. On the other hand, an asymmetric magnetic field profile accompanied with a linearly decreasing velocity is indicative of overall cross-section expansion. Both, the concepts of expansion and distortion, are closely related to the focus of this work.

The in-situ analysis can now be tested using remote sensing observations from the SECCHI imagers [Howard et al., 2008] aboard the STEREO mission [Kaiser et al., 2008], which image the ICMEs at the same locations as the in-situ observations in the heliosphere. On the solar side, the SDO mission provides high-resolution observations of the solar corona and the photosphere for the understanding of solar dynamics. The EUV disk imagers and white light coronagraphs on STEREO can currently provide side views of the CME initiation and follow the CME all the way to 1 AU and beyond.

Forward modeling concepts, such as that of Thernisien et al. [2006]; Thernisien [2011], can be used to fit the CME flux rope in imaging observations from multiple vantage points and provide geometrical information, such as orientation, propagation direction and 3D structure. The model results become increasingly more robust when observations from different viewpoints are used. The analysis uses images from the coronagraphs on STEREO and SOHO. For simplicity and to keep the number of free parameters to a minimum, this model assumes that the flux-rope has a circular cross-section. However, this may not always be correct for the propagation of CMEs in the interplanetary medium.

Recently, Savani et al. [2011] derived a geometrical semi-empirical aspect ratio (χ) for the CME's cross-section (i.e. relationship between major and minor radius) given by the

expression,

$$\chi = \frac{R(r_0/L_0)}{r_0 + A(R - L_0)} \tag{2}$$

where R is distance from the Sun, r_0 is the initial circular radius ($\sim 1 R_S$), L_0 is the initial distance from the Sun ($\sim 2 R_S$), and A is the constant rate of expansion. The minor radius is given by

$$Minor\ Radius = 2(r_0 + A(R - L_0)). \tag{3}$$

Interestingly, based on equation (2), by 0.5- 1.0 AU, the predicted aspect ratio tents to a fixed value. It would mean that the cross section morphology should remain constant.

The orientation of the CME (and later of the MC) is also little-understood. Yurchyshyn [2008] speculates that the axis of the ejecta may rotate towards the heliospheric current sheet. Rotation in the low corona is observed relatively frequently [Green et al., 2002] but it was never seen in the outer corona until recently. Vourlidas et al. [2011] provided the first evidence of a CME rotation in the middle and outer corona.

Therefore, analysis of CME images can provide information on the early stages of MCs, such as the expansion of the CME cross-section, its global structure and the orientation of the flux rope. This information can then be compared with in situ observations of the same MC allowing us to better understand the role played by expansion and rotation in the orientation of the CME at 1 AU. This is very important to accurately forecast the geo-effectiveness of CMEs.

In this paper, we have chosen to analyze the strongly rotating event, on June 16, 2010, reported by Vourlidas et al. [2011] (Paper I, henceforth). It exhibited a very clear flux-rope structure in the coronagraph and heliospheric imager observations from SEC-

CHI/STEREO and LASCO/SOHO, and it was in-situ detected clearly by both MESSENGER at 0.5 AU and Wind at 1 AU. The event belongs to the class of 'stealth CMEs' [Robbrecht et al., 2009] and therefore it has an extremely weak low corona signatures, no flares, and propagates slowly. The relative locations of the STEREO and MESSENGER spacecraft, and Earth (Wind and SOHO) provide a very desirable configuration for analyzing the kinematics and dynamics of this event.

For the analysis, we use data from SDO, STEREO, SOHO, Wind and MESSENGER, and several techniques, such as the Graduated Cylindrical Shell (GCS) [Thernisien et al., 2006], and in-situ analytical models with and without distortion in the cross section [Hidalgo et al., 2002; Nieves-Chinchilla et al., 2009; Lepping et al., 1990]. The focus of the paper is the rate of cross-section expansion and distortion of the flux rope, but we will also demonstrate that single view-point observations could lead to confusion in interpreting the observations. Only with the use of multispacecraft/multipoint analysis, we can understand the detailed evolution of these ICMEs.

The paper is organized as follows. We present the remote and in-situ observations in § 2 and their analysis in § 3. We offer a set of scenarios that are consistent with the observations in § 4 and discuss the implications for the CME expansion in § 5. We conclude in § 6.

2. Observations of the 16 June, 2010 CME

On June 16, 2010, an Earth-directed CME was observed by the STEREO-SECCHI and SOHO-LASCO telescopes. Between June 16 and 21 of 2010, the STEREO spacecraft and Earth (SOHO and Wind spacecraft) are in a configuration such that the angle between Earth and STEREO B (STB) is -70^o and between Earth and STEREO A (STA) is 74^o.

Figure 1 shows the positions of STEREO A and B spacecraft with respect to Earth in the ecliptic plane. The position of the MESSENGER spacecraft also appears in the figure at a distance of $\sim$0.5 AU, and at an angle of -20^o from the Sun-Earth line towards STB.

2.1. Remote Sensing Observations

The CME was observed remotely until it reached Earth on June 21, 7:20 UT. The CME initiation was observed by the EUV imagers aboard three spacecraft; SDO, STA and STB. These and the inner corona observations of the CME are discussed in detail in Paper I. We give only a brief summary here.

The CME was first observed in the SECCHI COR1-A and -B fields of view on 16 June 2010 at 06:05 UT. The CME was a typical 'stealth CME' event [Robbrecht et al., 2009]. It was not associated with any obvious low coronal activity on the disk such as a flare or filament eruption. However, the EUVI-A and B telescopes detected outflowing material, off the Earth-facing solar limb, in 304$\mathring{A}$ and 195$\mathring{A}$ images. Thanks to the observations, we were able to identify the source region in the SDO/AIA and HMI observations. The event originated from an extended quiet Sun filament channel located close to the central meridian and oriented at 38° CCW from the solar equator (Figure 2b). A careful inspection of the AIA images revealed a weak post-CME loop arcade after 12:11 UT.

Since it was Earth-directed, the CME appeared as a partial-halo in LASCO and had the well-known white light flux rope appearance (e.g., Chen et al. [1997], Vourlidas et al. [2000]) in the SECCHI-A and B coronagraphs. It emerged close to the equator in COR1 with a very similar morphology in the COR1-A and B views. However its morphology and location changed significantly as it propagated through the COR2 fields of view, losing some of its symmetry between the A and B views (Figure 2 a-f). The COR2 and HI

observations show a clear V structure at the back of the CME which is thought to be indicative of the trailing part of the ejected flux rope [Shiota et al., 2005]. In the COR2 and HI1 fields of view, the CME over-expands (Paper I) and flattens from the more circular appearance in COR1. This peculiar behavior is uncommon at these heights but it can be explained by rotation of the structure away from the sky plane without the need to invoke any distortion due to interaction with the solar wind (i.e., 'pancaking'). The observations through the edge of the COR2 field of view are consistent with a rotation rate of 60° per day (Paper I). Table 1 gives the time at which the CME is first observed in each instrument.

2.2. In-situ observations

On 21 June 2011 at 7:12 UT, the front of this ICME encountered the Wind spacecraft. At this time, the magnetometer MFI [Lepping et al., 1995] observed a slight increase in the magnetic field magnitude up to a maximum of 8.6 nT, in contrast with the ambient solar wind field of 2.5 nT (Figure 3). A large change was observed in the X-component of the magnetic field that indicates a flux rope topology. The magnetic cloud region is defined by the low proton plasma temperature as measured by the SWE instrument [Ogilvie et al., 1995]. The rear boundary was identified mainly based on the proton plasma temperature profile. The solar wind bulk velocity showed a typical profile for an expanding flux rope. The expansion velocity without any correction was ∼30 km/s, which according to Owens et al. [2005] is agreement with the transit velocity.

On the bottom half of Figure 3, the electron Pitch Angle Distribution (PAD) at 116.1 and 193.4 eV show an increase of the electron flux at 0° that suggest magnetic field lines connected to the Sun for one of the CME's legs. This in-situ observation agrees with the

remote sensing observations that suggest a disconnection from one of the footpoints (see Paper I).

Finally, we point out an increase in electrons at 0^o pitch angle inside the magnetic cloud. This increase is associated with a slight increase in the density. However, there does not appear to be any corresponding solar activity at the source region at this time.

The MESSENGER mission [Solomon et al., 2001] has become the first mission to orbit around Mercury. The scientific objectives of the MESSENGER mission are not focused on interplanetary or solar studies. However, its proximity to the Sun and its occasional ability to provide an advantageous multispacecraft configuration for some solar transient events has made MESSENGER an important mission for ICME studies. The event here is such an example.

Between 19 June 2011 10:05 and 20 June 2011 2:24 UT, the MESSENGER spacecraft was in the ambient solar wind. The onboard magnetometer (MAG), [Anderson et al., 2007], recorded the data in Figure 1. The signatures in the magnetic field magnitude and components show the obvious profile of a flux rope. The MESSENGER mission does not provide plasma parameters, so this event can not be identified as a MC with all certainty, and its boundaries are ambiguous. This fact is important because different time intervals provide different flux-rope orientations and may lead to different scenarios as we will see later.

3. Analysis and Results

Our goal is to examine the dynamical evolution during the CME's interplanetary propagation in order to understand the heliospheric expansion of these flux ropes. To this end, we have carried out an analysis using a number of different techniques and models

available in the literature. Specifically, we have used three methods to obtain information from the data. First, we measured the evolution of the CME envelope as a function of heliocentric distance directly from the images. This so called 'height-time' method provided the rate of expansion of the front with respect to the rear edge. Second, we applied the forward modeling technique of Thernisien et al. [2006] that uses imaging observations from multiple vantage points to derive the orientation, propagation and geometry of the erupting structure at different times. Third, we fitted the in-situ magnetic field data with two analytical models to derive the orientation of the MC. The first model assumed a circular cross-section while the second model allowed possible distortions in the MC cross-section.

3.1. Height-Time Measurements of the CME Envelope

This is the most common method of extracting information from HI/coronagraph images through direct measurements of the height versus time of the feature of interest. Because the visible emission is optically thin, these measurements always refer to quantities projected onto the plane of the image. Here, we measure four distinct features of the CME: the leading and trailing edges, and the two furthest latitudinal extents of its flanks. We define the trailing edge as the apex of the V-feature (Figure 2). From the measurement of the leading edge, we determine the velocity and position angle of the CME (Table 1). We use these measurements to characterize the dimensions of the CME, by calculating the front elongation and the CME diameters parallel and perpendicular to its propagation. These parameters are represented schematically in Figure 4.

Although direct measurements of CMEs are relatively easy to carry out they must be interpreted with care because they are subject to projection effects, which depend on the

CME orientation. For example, the perpendicular (to the propagation direction) diameter is an upper limit to the actual cross-section of the CME. If the CME is oriented face-on, as in Figure 5a then the perpendicular diameter is the width of the CME. If the CME is oriented edge-on (Figure 5b), the perpendicular diameter is the actual cross-section of the CME. For any other orientation between these two extremes, the perpendicular diameter will be larger than the CME cross-section. Generally, it is difficult to correct for this projection since we do not know *a priori* how the CME is projected onto the plane of the sky. A similar argument can be made for the parallel (along the propagation direction) diameter. Contrary to the case for the perpendicular diameter, the parallel diameter is the lower bound of the CME cross-section. If the CME is oriented in the plane of the image then the parallel diameter will be the cross-section. If the CME is oriented out of the plane of the image then the parallel diameter will be shortened by the projection. Therefore, the parallel diameter will always be less than or equal to the actual CME cross-section.

The height-time measurements are shown in Figure 6a. They suggest that the expansion of the CME diameter, whether perpendicular or parallel to the propagation direction, is not linear. However, we cannot be sure if this is a real or a projection effect until we correct for projection effects. To properly estimate those, we need to derive the flux-rope orientation as follows.

3.2. GCS model

The Graduated Cylindrical Shell model (GCS) was developed by Thernisien et al. [2006, 2009] to provide a means for analyzing for 3D morphology, position and kinematics of CMEs in white-light remote sensing observations. The GCS model uses forward-

modeling techniques that allows the user to fit a geometric model of a flux rope to CME observations. The geometry of the empirical flux rope model is depicted in Figure 5. The technique allows variation in the Carrington longitude (Φ_{GCS}), heliographic latitude of the Solar Region (SR, previously identify in Paper I) (Θ_{CGS}) and tilt angle of the SR neutral line (γ_{GCS}) around the axis of symmetry of the model. The origin is fixed at the center of the Sun. The size of the flux rope model is controlled by three parameters that define the apex height, foot point separation and the radius of the outer shell. The main assumption is the circular cross-section. The details of the model as well as the derivation of many secondary parameters used in this paper are discussed by Thernisien [2011].

The GCS technique has been used to derive the orientation of the flux rope in remote sensing data and the results agreed well with in-situ observations [Lynch et al., 2010; Rodriguez et al., 2011]. We applied this model in Paper I and found that the CME rotates in the middle corona. Here, we extend the results of Paper I further into interplanetary space for comparison with the in-situ data. We fit the GCS model to all available coronagraphic images from the time of the CME emergence in the COR1 field of view until a distance of $\sim$ 0.7 AU in the HI2 images. From the model fit we are able to estimate the 3D position and size of the CME at each observed height. Figure 6b (top) shows the ICME direction of propagation and width, derived by the GCS model fitting, projected to the ecliptic. Figure 6b (bottom) shows the same results projected on a plane normal to the ecliptic. Our 3D reconstruction suggests that different parts of the CME may have passed over the MESSENGER spacecraft and Earth.

The GCS technique is of limited use for studying CME distortion due to interactions with the solar wind since the empirically defined flux rope model has a circular cross-

section. Regarding the rotation of the structure, we note that, given the symmetry in the two STEREO views, the third view from LASCO is critical for restricting the CME orientation. The CME is only visible in the LASCO-C3 data only out to $\sim$32 $R_{\odot}$. Thus the GCS model becomes more uncertain at the distance of MESSENGER to in-situ observations.

3.3. In-situ analysis

Several models have been presented in the literature since Burlaga et al. [1981] defined magnetic clouds. The MC model developed by Lepping et al. [1990] was the first to attempt to obtain an understanding of the basic structures although its assumptions are very restrictive. The Lunquist [1950] solution for a cylindrical approximation for a force-free torus has represented a framework for the understanding of interplanetary magnetic cloud. It provides an approach of interpretation for the MC topologies and orientations. However, by definition, it can not address distortions of the flux rope cross-section.

The other analytical model used in this paper was published by Hidalgo et al. [2002] and further developed by Nieves-Chinchilla et al. [2009]. Two characteristics distinguish this model from the others in the literature: 1) none force-free condition is assumed, and, 2) an elliptical cylindrical coordinate system is chosen to resolve the Maxwell equations (Figure 5a in Nieves-Chinchilla et al. [2011]). Both of these conditions significantly relax the requirements of the model flux rope and allow more general solutions with serious implications on the global geometry of the fitted ICME. The first condition has implications for the overall picture of the CME/ICME evolution in the interplanetary medium. Locally, at 1 AU, the assumption that the system is under a force free condition could be correct. However, we treat the problem more generally in order to understand the inter-

planetary expansion and evolution of the ICME. So we relax the force free condition, in order to study the evolution of the early stages of the ICME. The second condition has an impact directly on the structure's geometry. A proper elliptical coordinate system allows us to consider cross-section distortion. The magnetic field components in this coordinate system (called MC coordinate system) are obtained under the cylindrical approximation and are given by

$$B_y = B_y^0 - a j_\eta \mu_0 \sinh\eta E[\varphi, -1/\sinh^2\eta]$$

$$B_\varphi = a\mu_0 j_y^0 \frac{\sinh\eta}{\sqrt{\cosh^2\eta - \cos^2\varphi}}$$

where $E[\varphi, -1/\sinh^2\eta]$ is the elliptic integral of second kind and it is numerically solved for in the algorithm [Nieves-Chinchilla et al., 2009]. The characteristics of the parameters are described by Hidalgo et al. [2002] and Nieves-Chinchilla et al. [2009] for the axial magnetic field component (B_y) and poloidal magnetic field component (B_φ). The spacecraft trajectory inside of the magnetic cloud defines the poloidal angle (φ) around the axial coordinate (Figure 5b in [Nieves-Chinchilla et al., 2011]), and the focus (a) of the ellipse that defines the MC cross section. Therefore, model parameters that define the physical characteristics and MC morphology are: radial and axial current density (j_η, j_0), axial magnetic field (B_y^0), and distortion (η). Moreover, from the projection of the spacecraft coordinate system (in this case, RTN coordinates), we are able to get information about the MC orientation: longitude (ϕ^{model}), latitude (θ^{model}), *local propagation angle* (ξ^{model}), and the impact parameter (y_0).

All fit parameters from the non force-free (NFF) model are included in table 2. The comparable results from the force-free (FF) model are also included. The angles are defined as longitude (ϕ^{model}) with the ϕ^{model}=0^o in the Earth-Sun direction, and, latitude

(θ^{model}), from -90^o to 90^o (where positive values represent north of the ecliptic plane). The coordinate system is observer-centric. To be consistent with the remote sensing analysis we define positive values of the CME/ICME axis *tilt* as clockwise rotation around the Sun-Earth line, centered on the Sun.

The purpose of this model is not only to describe the morphology or geometry of the MC, but also to understand the physics inside of the CME/ICME by relaxing, in this case, the force free condition. Even though the non-force-free (NFF) model has larger number of free parameters and thus greater uncertainties, all the fitted parameter correspond to physical characteristic of the MC that can be tested, such as the local propagation angle, the direction into which the MC travels. In order to understand the distortion as a consequence of the interaction of the flux-rope with the ambient solar wind, the in-situ analysis must take into account that the spacecraft-ICME encounter is not always at the ICME front and thus, the cross-section major axis is not always perpendicular to the ecliptic plane (Figure 5b in Nieves-Chinchilla et al. [2011]).

In Figure 1, the data from MESSENGER and Wind are shown, along with the NFF model-fitting (smooth lines). In Table 1, we list the time intervals chosen for this analysis, the solar wind velocity and the maximum magnetic field magnitude in the analysis-interval. In the case of MESSENGER, the solar wind velocity is an estimated value from the CME ejection time and ICME arrival time since MESSENGER does not have solar wind instrumentation. Table 2 shows the whole set of fit parameters for the NFF model and the comparable parameters for the FF model. The obtained orientations for both models/data are in RTN coordinates. To simplify the interpretation, the Wind data has also been converted to RTN coordinates using the approximation: $B_x^{GSE} = -B_R$,

$B_y^{GSE} = -B_T$, and, $B_z^{GSE} = B_N$, which introduces an error that is significantly less than the uncertainties of the applied models.

Both time intervals selected for the MC boundaries are listed in table 1. In the case of the MESSENGER observations of this MC, the rear boundary seems to be clear but, we have at least two possible front boundaries. The results from the model fitting appear in Table 2. During interval 1 as well as interval 2, the differences in the axis orientation for the FF and NFF models could be due to the different geometrical approach used by the models. For interval 1 (shorter), the NFF model gives a longitude (ϕ_{NFF}^{model}=120^o) with a slight tilt (θ_{NFF}^{model}=-38^o). So, for interval 1, the $tilt_{NFF}^{model}$ is 38^o from the NFF model, and with the FF model, we get a slightly different value for the longitude, and the MC's axis is close to the ecliptic plane (ϕ_{FF}^{model}=128^o and $tilt_{FF}^{model}$=10^o). The schematic picture with the possible configuration is shown in Figure 7.

For the larger interval (interval 2) the front boundary is identified to be earlier, at 3:45 UT of 19 June 2010 (Table 1). The consequences of choosing this earlier start time are significant. In the case of the FF model, the longitude of the MC axis (ϕ_{FF}^{model}=167^o) and the latitude ($tilt_{FF}^{model}$=69^o) changed significantly compared to the results of the shorter interval. Likewise, for the NFF model, with a longitude (ϕ_{NFF}^{model}=144^o) and latitude ($tilt_{NFF}^{model}$=43^o), the change is also significant with a diminished goodness of fit. Furthermore, the discrepancies between the results of the two models increases for the second analysis-interval bringing into question its validity. However, in the case of the axial magnetic flux, the result from the FF model is $6.6 \cdot 10^{20}$ Mx and from the NFF model is $4.7 \cdot 10^{20}$ Mx, which is closer to the values obtained at 1 AU, Table 2. The difference between the two model results is due to the larger cross section area associated with the FF model.

We now focus on the Wind observations. Applying the same MC fit procedures, we found that the *tilt* angle is similar for both models: $tilt_{FF}^{model} = 6^o$ and $tilt_{NFF}^{model} = -14^o$, with respect to the ecliptic plane. However, the estimated longitude angles for the models differ by 32^o. For the FF model this implies that the spacecraft could have crossed close to the front of the MC, but the NFF model results suggest that the spacecraft could have crossed through the flank. It is important to keep this discrepancy in mind in order to create a scenario for the CME propagation in the solar wind.

One more parameter obtained with the NFF model should be discussed: the distortion (ϵ), in this case defined as minor axis over the major one. There is a discrepancy between the analysis results between Interval 1 (on MESSENGER data) with a value of 55% and Wind with a value of 86%. There is a closer agreement between Wind and the MESSENGER Interval-2, 86% and 96%, respectively.

4. Remote – In situ Comparisons: CME/ICME Rotation

Using on the SECCHI and LASCO remote observations and the Wind in situ data, we were able to confirm that the June 16 CME was Earth directed. Initially we selected this event as suitable for studying cross-section expansion because of its well-defined flux-rope structure in the images, the lack of other interfering events in the interplanetary medium, and the apparent slight tilt of the ICME on the ecliptic plane. However, we uncovered several peculiarities as the study progressed.

The first peculiarity is related to the lack of a clear source region. This event had the typical characteristics of 'stealth CMEs' [Robbrecht et al., 2009; Ma et al., 2010]. Only thanks to the side views from the EUVI telescopes, we were able to identify the source region and thus determine the orientation of the pre-eruption arcade using PFSS extrap-

olations (details on Paper I). The subsequent GCS fits uncover an even more unexpected peculiarity. They showed a large rotation in the middle corona that we were able to follow to the location of the MESSENGER in this paper. Figure 8c compares the tilt of the CME/ICME as derived from the remote and in-situ observations. The tilt variation, is measured relative to the solar equator (a positive angle reflects clockwise rotation as viewed from Earth). At the location of MESSENGER, we see that, the tilt angle obtained by the GCS technique differs by $\sim 100^{\circ}$ from the orientation derived by the analytical in-situ models of the MESSENGER magnetometer data. This is the third peculiarity and we can propose three possible explanations for this discrepancy.

1. *CME counter-rotation.* As we have pointed out in Paper I, the CME propagates symmetrically relative to the SECCHI instruments and hence its appearance is very similar from the SECCHI-A or -B viewpoints. We are able to establish the CME rotation reliably thanks to the third eye-views provided by the LASCO coronagraphs. After the CME exits the C3 field of view on June 17^{th} 08:09 UT at a distance of 32 $R_{\odot}$, orientation of the CME from the GCS fit, becomes somewhat ambiguous. Although we can only derive the absolute tilt of the flux rope relative to the plane of symmetry between the STA and STB we cannot tell whether the structure is tilted forward or backward relative to that plane. In Figure 8c we make the straightforward assumption that the CME maintains its counterclockwise rotation after leaving the C3 field of view. But what if the CME decides to oscillate and hence rotate in the opposite sense in the outer corona? Practically speaking, we should be able to see the CME rotating through the 0° by an increase, followed by a decrease, of its latitudinal width. Figure 8b shows the CME width determined by the GCS model and by the perpendicular height-time measurement. It is

a fact that the emission at the CME boundaries weakens as it expands making it difficult to derive the CME orientation with confidence at these large distances. Therefore, it is conceivable that the CME rotated clockwise between June 17-19. In that case, the tilt in HI2 would be 55° and would match the MESSENGER in-situ reconstructions very well (white triangles in Figure 8).

To define better this oscillatory scenario, we fitted the values obtained with the GCS technique until day 17.33 (x_c), to a function:

$$angle = A \sin \frac{\pi(x - x_c)}{w} \tag{5}$$

where A is the amplitude in the angle equal to 68.0 $\pm$ 7.6, and w is the frequency in the change of the rotation sense. The value for w parameter is 2.0$\pm$0.5 decimal day. The profile obtained with these parameters is depicted in the Figure 8b with a dash gray line. The fit matches the MESSENGER in-situ tilt values. Although we do not consider it further here, we have to accept the 'damped-oscillation' as a viable, and intriguing scenario for the CME behavior in the heliosphere. Further work should hopefully clarify this issue.

2. *CME keeps rotating.* Alternatively, we can assume that the CME keeps rotating throughout the HI1 and HI2 fields of view at the same rate as measured in the coronagraph ($\sim 90°$ day^{-1}). In that case, the CME would rotate another 180° by the time it reaches MESSENGER on June 19, 12UT. It will have a tilt of around 90°, which is in relatively good agreement to the in-situ results.

3. *Inaccurate in-situ derived tilts.* Finally, the in-situ reconstructions may be inaccurate. Because the MESSENGER mission does not carry a solar wind plasma instrument so we are not able to delineate accurately the MC boundaries. However, the MC ori-

entation will depend on the chosen boundaries. To account for that, we have tried two likely intervals and used two analytical models to derive the MC orientation as discussed in § 3.3.

5. Remote – In situ Comparisons: Expansion

After our discussion of the two rotation scenario for our CME, we turn our attention to the main subject of this paper; namely, the analysis of the evolution of the CME cross section using the height-time and GCS measurements described in Section 3.1. We are in the unique position to be able to derive true (deprojected) quantities for the CME cross sections parallel and perpendicular to its propagation direction because we have three-dimensional information on the CME size and orientation. First, we derive the deprojected perpendicular diameter from the diameter determined by the height-time measurements using the width and *tilt* of the CME from the GCS analysis. The geometry, as viewed by an observer along the POS, is shown in Figure 8a. The deprojected perpendicular diameter, D_p^c, is then

$$D_p^c = \frac{D_p^d - W\cos tilt}{\sin tilt} \tag{6}$$

where *tilt* is γ^{GCS} and W is the CME width (W, Figure 5). The projected (black circles) and deprojected (white circles) values are plotted in Figure 8b. Also plotted are the GCS true (white stars) and projected (black stars) widths. The very small D_p^c values between June 17-18 are due to the very high inclination ($\sim 90°$) of the CME flux rope which causes divergence of the correction in equation (5). In other words, we do not have information on the perpedicular diameter when the CME axis lies on the POS. At later times, the CME seems to rotate back towards the ecliptic and we can again follow the evolution of

457 D_p^c. However, those later measurements are based on two-viewpoint observations which
458 introduce some ambivalence on the sign of the CME tilt as we discussed in the previous
459 section. So, we choose to focus on the more reliable three-viewpoint data (SECCHI +
460 LASCO) for the analysis of the CME expansion.

461 Figure 9 shows the CME evolution in the inner corona when it was observed by both
462 SECCHI and LASCO. We present here only the SECCHI-A measurements, since the CME
463 propagation direction is 20° away from the Sun-Earth line, hence closer to the plane of sky
464 (POS) of STA (Figure 6b (top)). The measurements cover an 18-hour period, from the first
465 CME observation to the end of 16 June. From bottom to top, we plot the perpendicular
466 and parallel diameters, the tilt of the CME derived from the GCS fit, and finally the
467 ratio of perpendicular to parallel diameters. Note that the perpendicular diameter has
468 been corrected for the effects of projection and rotation as discussed above. We did not
469 deproject the parallel diameters since the CME propagates along the SECCHI-A POS and
470 the projection effects are minimal. The ratio of the two diameters provides a measure of
471 the distortion of the CME flux rope during its heliospheric propagation. When it is close
472 to unity, the flux rope has a circular shape. When the distortion ratio is below one, then
473 the CME is elongated along its propagation direction which is not a common occurrence
474 in propagation models. Many MHD models of CME propagation predict that the CME
475 should 'pancake', its distortion should be higher than unity, due to its interaction with
476 the solar wind and even if it is expanding self-similarly [Riley & Crooker, 2004].

477 At first sight, our projected height-time measurements appear to support that expec-
478 tation (black circles in Figure 9 top). The (projected) distortion is as high as 1.5 early
479 on and although it becomes approximately one around day 16.5, it quickly returns above

unity. However, the results change as soon as we correct for the projection effects (white stars). The corrected observations suggest that the flux-rope is distorted mainly in the propagation direction by as much as a factor of two more than in the perpendicular direction. It seems, therefore, that projection effects can affect significantly the analysis of imaging observations based on 'point-and-click' methods, such as height-time measurements. Every effort should be made to estimate the three-dimensional configuration of the structures and to attempt projection corrections before reaching any conclusions.

We now return our attention to the variation of the two diameters, parallel and perpendicular. We fit the measurements between June 16 and 17 (Figure 9 as a function of heliocentric distance using equation (1), where x is the heliocentric distance. Then we extrapolate that function to distances beyond 1 AU to compare with the other imaging measurements and the in-situ models. The results are plotted in Figure 10 with red lines. We also plot the Bothmer & Schwenn [1998] empirical law (blue lines) for comparison. In the same figure, we plot the projected and corrected height-time measurements (black dots and white stars, respectively), the predicted perpendicular diameters based on the Savani et al. [2011] results (orange dots) and finally, the values obtained from the analytical in-situ models at 0.5 and 1 AU (red/green/blue symbols for different time intervals, see also Tables 1 and 2).

The conclusions are straighforward in the case of the parallel diameter. We find a rate of expansion, $D_{par} = 0.20 \pm 0.04 x^{0.74 \pm 0.02}$, very similar to Bothmer & Schwenn [1998] and Savani et al. [2009]. Our results agree very well with the NFF model with Interval-2 for both MESSENGER (at 0.5 AU) and Wind (at 1 AU).

In the case of the perpendicular diameter, the agreement among the various models is less satisfactory. It is clear that the projected height-time measurements and the Savani et al. [2011] results, which are based on projected measurements are inconsistent with both in-situ models and the empirical law. This is hardly surprising since we have established that projected quantities are unreliable. Indeed, the deprojected measurements produce a fit, $D_{perp} = 0.15 \pm 0.04x^{0.89\pm0.09}$, consistent with the Interval-2 NFF model for MESSENGER and consistent with the corrected measurements in the HI1 and 2 fields of view (which we choose not to include in the fit). At 1 AU our expansion fit predicts a smaller diameter than the in-situ models. We do not know the reason for this discrepancy. It may be that a single exponent is not a good description for the evolution of the perpendicular diameter in the inner heliosphere. The deprojected measurements around 0.5 AU suggest a sharper slope than 0.89, for example. Alternatively, Wind could be crossing a different part of the CME compared to MESSENGER which in turn may be expanding at a different rate. The imaging measurements are unlikely to be sensitive to such intra-structure variations because of the large line of sight integration.

Finally, we should clarify how we use equations 2 and 3 from Savani et al. [2011] to obtain a prediction for the variation of the perperdicular diameter. The minor radius in Savani et al. [2011] corresponds to our parallel diameter. Since their parallel diameter is consistent with our results and the Bothmer & Schwenn [1998] empirical relationship, we can use it to obtain the rate of expansion, A, from equation 3. Adopting the standard values for r_0 and L_0 (see section § 1), we find A=0.115. According to Savani et al. [2011], this value suggests that the perpendicular diameter (their major diameter) is five times larger than the minor diameter. Although these values (orange cicles in Figure 10) are in

agreement with Owens [2006] and Forsyth et al. [2006], they are in obvious disagreement with both our corrected results and with the in-situ analytical models. The reason is obvious: projection effects must be taken into account for any measurements extracted from imaging observations.

6. Summary and Conclusions

In this paper, we investigate the rate of expansion of a CME both parallel and perpendicular to its direction of propagation. We use imaging observations from the SOHO and STEREO spacecraft, magnetometer data from the MESSENGER mission and a complete set of plasma and magnetic field data from the Wind spacecraft. Thanks to the resulting comprehensive coverage, we are able to track the CME from its origin on June 16 to its impact on Earth on June 21, 2010 and derive its three-dimensional properties during that time interval. We selected this event because it was Earth-directed, and belonged to the class of 'stealth CMEs' which may be of interest to the space weather community.

The spatial configuration of these spacecraft allow us to link the remote observations to the in-situ data through the use of direct measurements and 3D reconstructions based on multipoint imaging and analytical in-situ models. This event, which initially appears to be a normal fluxrope-type CME, actually provides the first unambiguous evidence of CME rotation in the middle corona. The serendipity of the measured rotation (100°/day) necessitated a separate publication (Paper 1) and remains unexplained. To complicate matters, when the event was detected by MESSENGER as a MC, its orientation based on the in-situ measurements was 100° away from the orientation based on the imaging analysis. However, the imaging-derived orientation may have a sign ambiguity relative to the plane of symmetry of the SECCHI instruments. In Section 4, we offer two possible

explanations for this discrepancy: either (1) the CME continues to rotate at the same rate throughout its journey to 0.5 AU, or (2) the CME rotates back towards its pre-eruption orientation. Either scenario is plausible at this stage since we lack any other similar events to compare with. Theoretical modeling cannot guide us either. We are not aware of any CME propagation models that have looked at the effects of CME rotation or oscillation in the interplanetary space. Regarding the ability of this event to rotate so much, we can only point to the observation of disconnection of one of the CME legs (Paper I) that may have allowed the large-scale flux rope to rotate in the observed manner. Certainly, future modeling of this event will shed some light on which of the two scenario is more plausible.

Thanks to the three-dimensional information on the CME shape, the analysis of the CME cross section expansion, the main focus of our paper, can be corrected for the large rotation. Using a 'point-and-click' method, we obtain the parallel and perpendicular diameter (relative to the propagation plane) as a function of time and heliocentric distance. We then deproject this quantities using the tilt and width provided by the GCS fits to the structure. Our results can be summarized as follows:

• The distortion, defined as the ratio of the perpendicular to the parallel projected diameters, results in an elliptical shape consistent with model predictions of a pancaking CME. However, this picture changes completely once the measurements are corrected for projection effects. The corrected values show a distortion along the propagation plane, a 'stretching' of the CME, indicating, perhaps, a high-beta structure interaction with the ambient wind.

• The 3D analysis shows that the CME propagates close to the STEREO-A POS and hence the parallel diameter should not suffer projection effects. Indeed, we find that our

fit to the parallel diameter evolution as a function of distance is in very good agreement to the same in-situ model for 0.5 AU (MESSENGER) and 1 AU (Wind) and with the the empirical relationship of Bothmer & Schwenn [1998] for the interval of 0.3 to 4.5 AU. Hence, our analysis extends the validity of their model to about 5 solar radii.

• The perpendicular diameters need to be corrected for projection effects. As for the parallel diameter, we find that the rate of expansion agrees very well with the NFF model at MESSENGER but underpredicts at Wind. When comparing to the in-situ analytical models, we must point out that the Wind and MESSENGER spacecraft could be crossing different parts of the MC. Therefore, the discrepancy may indicate a varying rate of expansion at different CME locations or it may reflect a change in the expansion rate after 0.5 AU. There is a slight indication of the latter in the imaging measurements around 0.5 AU (Figure 10).

• Our rate of perpendicular expansion is slightly different from the Bothmer & Schwenn [1998] results. This discrepancy is probably unsurprising since Bothmer & Schwenn [1998] had no information on the latitudinal shape of the events in their analysis. They had to assume a constant circular shape. However, the SECCHI imaging observations since the launch of STEREO clearly show that the CME cross-section does not typically stay constant. The imaging analysis reported here suggests that the shape of the cross section can vary from elliptical to circular and back to elliptical as a function of heliocentric distance.

• Finally, our analysis does not provide evidence for CME pancaking away from the ecliptic plane despite model predictions. For example, Riley & Crooker [2004] predicts a progressive flattening in the perpendicular (to the ecliptic plane) direction with increasing

heliocentric distance. Our results are also in disagreement with geometrical arguments from Savani et al. [2011]. Their predictions fare worse than our own measurements. The Savani et al. [2011] equations predict a much faster expansion rate than observed either by the imaging instruments or derived from the in-situ data. This does not mean that pancaking does not take place during CME propagation. Our detailed investigation of the CME three-dimensional properties (direction, shape, tilt, and width) suggests, however, that the appearance of pancaking structures in images may be the results of projection effects, including CME rotation.

It is clear that further research is required to understand the latitudinal expansion of CMEs. In our case, the discrepancy between imaging and in-situ measurements is most pronounced during the last 0.5 AU of transit of the ICME to Earth. This discrepancy could be due to: 1) the projection effects are still not understood, and, 2) the Wind spacecraft is crossing different parts of the MC. Furthermore, the dynamic interaction with the ambient solar wind on the flanks could be different from the MC front [Odstrcil & Pizzo, 1999].

The analysis of the CME event on June 16^{th} provided an opportunity to combine the remote observations and in-situ data with different techniques and analytical models. Thanks to the multi-viewpoint observations we were able to uncover unexpected behavior (rotation) and account for it in our analysis. We present the first deprojected measurements of the variation of the CME size in the inner heliosphere. The results suggest that the parallel expansion obtained with data analysis techniques, models and geometrical predictions are in very good agreement. However, the evolution of the perpendicular expansion is still unclear. It is encouraging that the analysis done with the imaging obser-

vations, including corrections using the GCS technique, agrees with the in-situ analytical analysis. This result suggests that a combination of remote and in-situ observations has the potential to understand the dynamical interaction of CMEs with the solar wind and could be possible lead to the development of an analytical model. But first, our initial results need to be corroborated with a survey of events.

Acknowledgments. The work of R.C and A.V is supported by NASA contract S-13631-Y. SOHO is an international collaboration between NASA and ESA. LASCO was constructed by a consortium of institutions: NRL (USA), MPS (Germany), LAM (France) and Univ. of Bham (Birmingham, UK). The SECCHI data are produced by an international consortium of the NRL, LMSAL and NASA GSFC (USA), RAL and Univ. Bham (UK), MPS (Germany), CSL (Belgium), IOTA and IAS (France).

Anderson, B. J., Acuña, M. H., Lohr, D. A., Scheifele, J., Raval, A., Korth, H., & Slavin, J. A. (2007), The magnetometer instrument on MESSENGER, *Space Sci. Rev.*, 131(14), 417- 450, doi:10.1007/s11214-007-9246-7.

Bothmer, V., & Schwenn, R. (1998), The structure and origin of magnetic clouds in the solar wind, *Ann. Geophys.*, 16, 1- 24, doi:10.1007/s00585- 997-0001-x.

Burlaga, L., Sittler, E., Mariani, F., & Schwenn, R. (1981), Magnetic loop behind an interplanetary shock, *J. Geophys. Res.*, 86, 6673- 6684, doi:10.1029/JA086iA08p06673.

Burlaga, L. F. (1988), Magnetic Clouds and Force-Free Fields with Constant Alpha, *J. Geophys. Res., 93(A7)*, 7217- 7224, doi:10.1029/JA093iA07p07217.

Chen, J., Howard, R. A., Brueckner, G. E., et al. (1997), Evidence of an erupting magnetic flux rope: LASCO coronal mass ejection of 1997 April 13, *Astrophys. J.*, 490, L191.

638 Forsyth, R. J., Bothmer, V., Cid, C., et al. (2006), ICMEs in the inner heliosphere: Ori-
639 gin, evolution and propagation effects, *Space Sci. Rev.*, 123, 383- 416, doi:10.1007/s11214-
640 006-9022-0.

641 Gosling, J. T., Bame, S. J., McComas, D. J., & Phillips, J. L. (1990), Coronal mass
642 ejections and large geomagnetic storms, *Geophys. Res. Lett.*, 17(7), 901- 904.

643 Green, L. M., López fuentes, M. C., Mandrini, C. H., et al. (2002), The Magnetic Helicity
644 Budget of a cme-Prolific Active Region, *Solar Phys*, 208, 43.

645 Hidalgo, M. A., Nieves-Chinchilla, T., & Cid, C. (2002), Elliptical cross-section model
646 for the magnetic topology of magnetic clouds, *Geophys. Res. Lett.*, 29(13), 1637,
647 10.1029/2001GL013875, 2002.

648 Hidalgo, M. A., Blanco, J. J., Alvarez, F. J., & Nieves-Chinchilla, T. (2011), On
649 the relationship between magnetic clouds and the great geomagnetic storms associ-
650 ated with the period 1995-2006, *J. Atmos. Sol. Terr. Phys.*, 73, 1372- 1379.
651 dx.doi.org/10.1016/j.jastp.2011.02.017.

652 Hidalgo, M. A. & Nieves-Chinchilla, T., A global magnetic topology model for magnetic
653 clouds (I). Accepted for *Astrophysical Journal*.

654 Howard, R. A., Moses, J. D., Vourlidas, A., et al. (2008), Sun Earth Connection Coro-
655 nal and Heliospheric Investigation (SECCHI), *Space. Sci. Rev.*, 136(1- 4), 67- 115,
656 doi:10.1007/s11214-008-9341-4.

657 Hu, Q., & Sonnerup, B. U. Ö. (2002), Reconstruction of magnetic clouds in the
658 solar wind: Orientations and configurations, *J. Geophys. Res.*, 107(A7), 1142,
659 doi:10.1029/2001JA000293.

Kaiser, M. L., Kucera, T. A., Davila, J. M., et al. (2008), The STEREO Mission: An Introduction, *Space Sci. Rev.*, 136, 516, doi:10.1007/s11214-007-9277-0.

Lepping, R. P., Burlaga, L. F., & Jones, J. A. (1990), Magnetic field structure of interplanetary magnetic clouds at 1 AU, *J. Geophys. Res.*, 95(A8), 11,957.

Lepping, R. P., et al. (1995), The Wind Magnetic Field Investigation, *Space Sci. Rev.*, 71, 207- 229.

Lundquist, S., Magnetohydrostatic fields, *Ark., Fys.*, 2, 361, 1950.

Lynch, B. J., Antiochos, S. K., Li, Y., Luhmann, J. G., & DeVore, C. R. (2009), Rotation of Coronal Mass Ejections during Eruption, *Astrophys. J.*, 697, 1918.

Lynch, B. J., Li, Y., Thernisien, A. F. R., Robbrecht, E., Fisher, G. H., Luhmann, J. G., & Vourlidas, A. (2010), Sun to 1 AU propagation and evolution of a slow streamer-blowout coronal mass ejection, *J. Geophys. Res.*, 115, A07106, doi:10.1029/2009JA015099.

Ma, S., Attrill, G. D. R., Golub, L., & Lin, J. (2010), Statistical Study of Coronal Mass Ejections With and Without Distinct Low Coronal Signatures, *Astrophys. J.*, 722, 289. doi:10.1088/0004-637X/722/1/289.

Möstl, C., Miklenic, C., Farrugia, C. J., Temmer, M., Veronig, A., Galvin, A. B., Vršnak, B., & Biernat, H. K. (2008), Two-spacecraft reconstruction of a magnetic cloud and comparison to its solar source, *Ann. Geophys.*, 26, 3139- 3152, doi:10.5194/angeo-26-3139-2008.

Möstl, C., et al. (2009), Multispacecraft recovery of a magnetic cloud and its origin from magnetic reconnection on the Sun, *J. Geophys. Res.*, 114, A04102, doi:10.1029/2008JA013657.

Nieves-Chinchilla, T., Viñas, A.-F., &Hidalgo, M. A. 2009, Magnetic Field Profiles Within Magnetic Clouds: A Model-Approach, *Earth Moon and Planets*, 104, 109.

Nieves-Chinchilla, T., et al. (2011), Analysis and study of the in situ observation of the June 1st 2008 CME by STEREO, *J. Atmos. Sol. Terr. Phys.* doi:10.1016/j.jastp.2010.09.026, 73, 1348.

Odstrcil, D., & Pizzo, V. J. (1999), Distortion of the interplanetary magnetic field by three-dimensional propagation of coronal mass ejections in a structured solar wind, *J. Geophys. Res.*, 104, 28,225- 28,239, doi:10.1029/1999JA900319.

Ogilvie, K. W., et al. (1995), SWE, A Comprehensive Plasma Instrument for the Wind Spacecraft, *Space Sci. Rev.*, 71(14), 5577, doi:10.1007/ BF00751326.

Owens, M. J., Cargill, P. J., Pagel, C., Siscoe, G. L., & Crooker, N. U. (2005), Characteristic magnetic field and speed properties of interplanetary coronal mass ejections and their sheath regions, *J. Geophys. Res.*, 110, A12105, doi:10.1029/2005JA011343.

Owens, M. J. (2006), Magnetic cloud distortion resulting from propagation through a structured solar wind: Models and observations, *J. Geophys. Res.*, 111, A12109, doi:10.1029/2006JA011903.

Richardson, I. G., Cane, H. V., & Cliver, E. W. 2002. Sources of geomagnetic activity during nearly three solar cycles (1972-2000). *J. Geophys. Res.*, 107(A8), 1187, doi:10.1029/2001JA000504.

Riley, P., & Crooker, N. U. (2004), Kinematic Treatment of Coronal Mass Ejection Evolution in the Solar Wind, *Astrophys. J.*, 600, 1035.

Riley, P., Linker, J. A., Lionello, R., et al. 2004, Fitting flux ropes to a global MHD solution: a comparison of techniques, *J. Atmos. Sol. Terr. Phys.*, 66, 1321.

Robbrecht, E., Patsourakos, S., & Vourlidas, A. (2009), No Trace Left Behind: STEREO Observation of a Coronal Mass Ejection Without Low Coronal Signatures, *Astrophys. J.*, 701, 283.

Rodriguez, L., Mierla, M., Zhukov, A. N., West, M., & Kilpua, E. (2011), Linking Remote-Sensing and In Situ Observations of Coronal Mass Ejections Using STEREO, *Sol. Phys.*, 270, 561

Shiota, D., Isobe, H., Chen, P. F., et al. (2005), Self-Consistent Magnetohydrodynamic Modeling of a Coronal Mass Ejection, Coronal Dimming, and a Giant Cusp-shaped Arcade Formation, *Astrophys. J.*, 634, 663678, doi:10.1086/496943.

Solomon, S. C., et al. (2001), The MESSENGER mission to Mercury: scientific objectives and implementation, *Planet. Space Sci.*, 49(14- 15), 1445- 1465.

Savani, N. P., Rouillard, A. P., Davies, J. A., et al. (2009), The radial width of a Coronal Mass Ejection between 0.1 and 0.4 AU estimated from the Heliospheric Imager on STEREO, *Ann. Geophys.*, 27(11), 4349- 4358.

Savani, N. P., Owens, M. J., Rouillard, A. P., Forsyth, R. J., Kusano, K., Shiota, D., & Kataoka, R. (2011), Evolution of Coronal Mass Ejection Morphology with Increasing Heliocentric Distance. I. Geometrical Analysis, *Astrophys. J.* 731, 109.

Schrijver, C. .J (2001), Simulations of the Photospheric Magnetic Activity and Outer Atmospheric Radiative Losses of Cool Stars Based on Characteristics of the Solar Magnetic Field, *Astrophys. J.*, 547, 475.

Thernisien, A. F. R., Howard, R. A., & Vourlidas, A. (2006), Modeling of Flux Rope Coronal Mass Ejections, *Astrophys. J.*, 652, 763.

727 Thernisien, A., Vourlidas, A., & Howard, R. A. (2009), Forward Modeling of Coronal
728 Mass Ejections Using STEREO/SECCHI Data, *Sol. Phys.*, 256, 111.

729 Thernisien, A. (2011), Implementation of the Graduated Cylindrical Shell Model for the
730 Three-dimensional Reconstruction of Coronal Mass Ejections, *The Astrophys. J. Supp.*
731 *S.*, 194:33 (6pp), doi:10.1088/0067-0049/194/2/33.

732 Vourlidas, A., Subramanian, P., Dere, K. P., & Howard, R. A. (2000), Large-angle spec-
733 trometric coronagraph measurements of the energetics of coronal mass ejections, *Astro-*
734 *phys. J.*, 534, 456467.

735 Vourlidas, A., Colaninno, R., Nieves-Chinchilla, T., & Stenborg, G. (2011), The First Ob-
736 servation of a Rapidly Rotating Coronal Mass Ejection in the Middle Corona, *Astrophys.*
737 *J. Lett.*, 733, L23- L28, doi:10.1088/2041- 8205/733/2/L23.

738 Yashiro, S., Gopalswamy, N., Michalek, G. St. Cyr, O. C., Plunkett, S. P., Rich, N. B.,
739 & Howard, R. A. (2004), A catalog of white light coronal mass ejections observed by the
740 SOHO spacecraft, *J. Geophys. Res.*, 109, A07105, doi:10.1029/2003JA010282.

741 Yurchyshyn, V. (2008), Relationship between EIT Posteruption Arcades, Coronal Mass
742 Ejections, the Coronal Neutral Line, and Magnetic Clouds, *Astrophys. J.*, 675, L49.

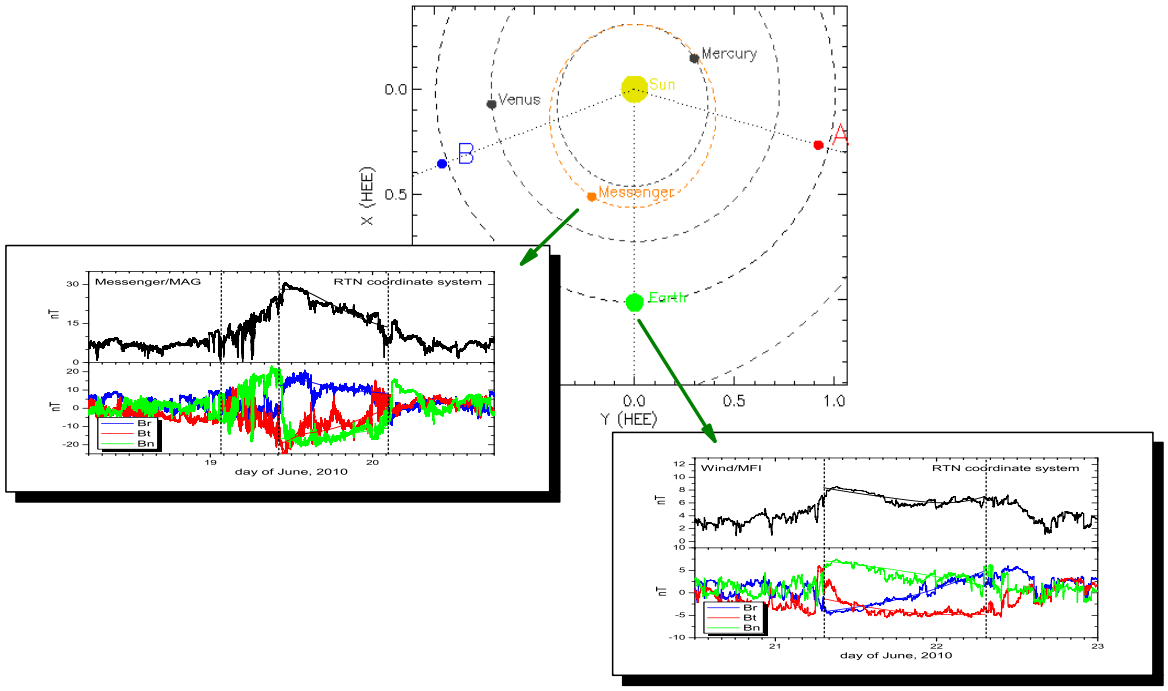

Figure 1. In the center, the positions of the STEREO A (red), STEREO B (blue), MESSENGER (orange), and Earth (green) depicted in the ecliptic plane on 16 June 2010. These missions provide us the data collected for the multipoint analysis of the single CME of June 16, 2010. The STEREO A and B spacecraft are at -74^o and 70^o from Earth, respectively. The MESSENGER spacecraft is at r $\sim$ 0.5 AU and at a -20^o angle with respect to the Earth-Sun line. SOHO and Wind are near Earth. Indicated with green arrows, two different set of panels for the in-situ magnetic field magnitude and components data and fitting with the NFF model are shown. On the bottom, from the Wind/MFI instrument and, on the left, the MESSENGER/MAG instrument.

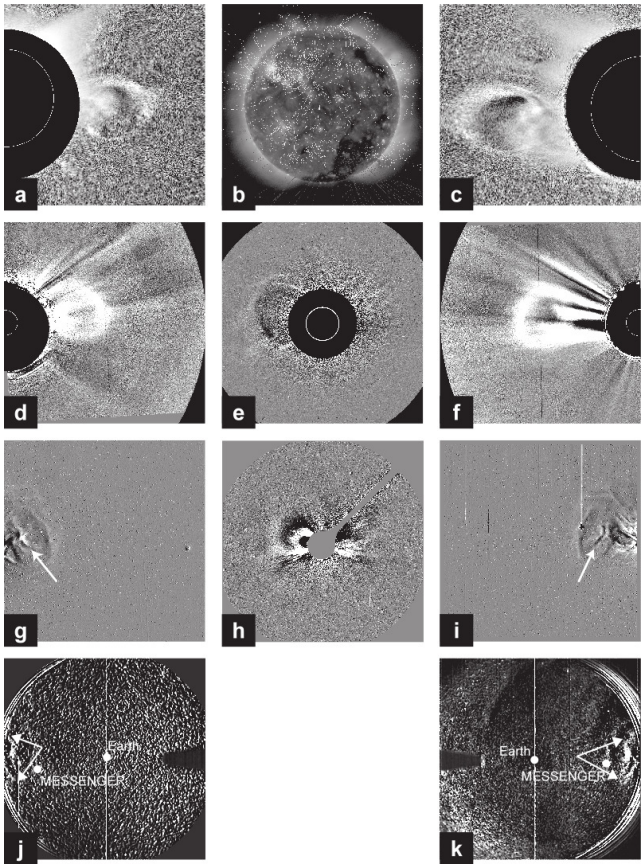

Figure 2. The left, center and right columns show images from the perspective of STEREO B, Earth, and STEREO A, respectively. (a, c) SECCHI COR1 images at 2010 June 16 12:10 UT. The CME emerging from a southern source region. (b) SDO AIA 193Å image at 2010 June 16 23:55:30 UT with superimposed field lines from a PFSS extrapolation. The CME source region is located mid-disk in the Southern hemisphere. (d, f) SECCHI COR2 images at 2010 June 16 18:24 UT. The CME has lost some of its symmetry from COR1 indicating non-radial motion. (e) LASCO C2 image at 2010 June 16 18:27 UT. LASCO images are critical for accurately obtaining the CME orientation. (g, i) SECCHI HI-1 images at 2010 June 17 09:29 UT. The CME front appears flattened with an elliptical cross-section. (h) LASCO C3 image at 2010 June 17 09:17 UT. The CME is expanding predominately to the north following a non-radial propagation path. (j, k) SECCHI HI-2 images at 2010 June 18 18:09 showing the CME front (highlighted with arrows) in relation to MESSENGER and EARTH.

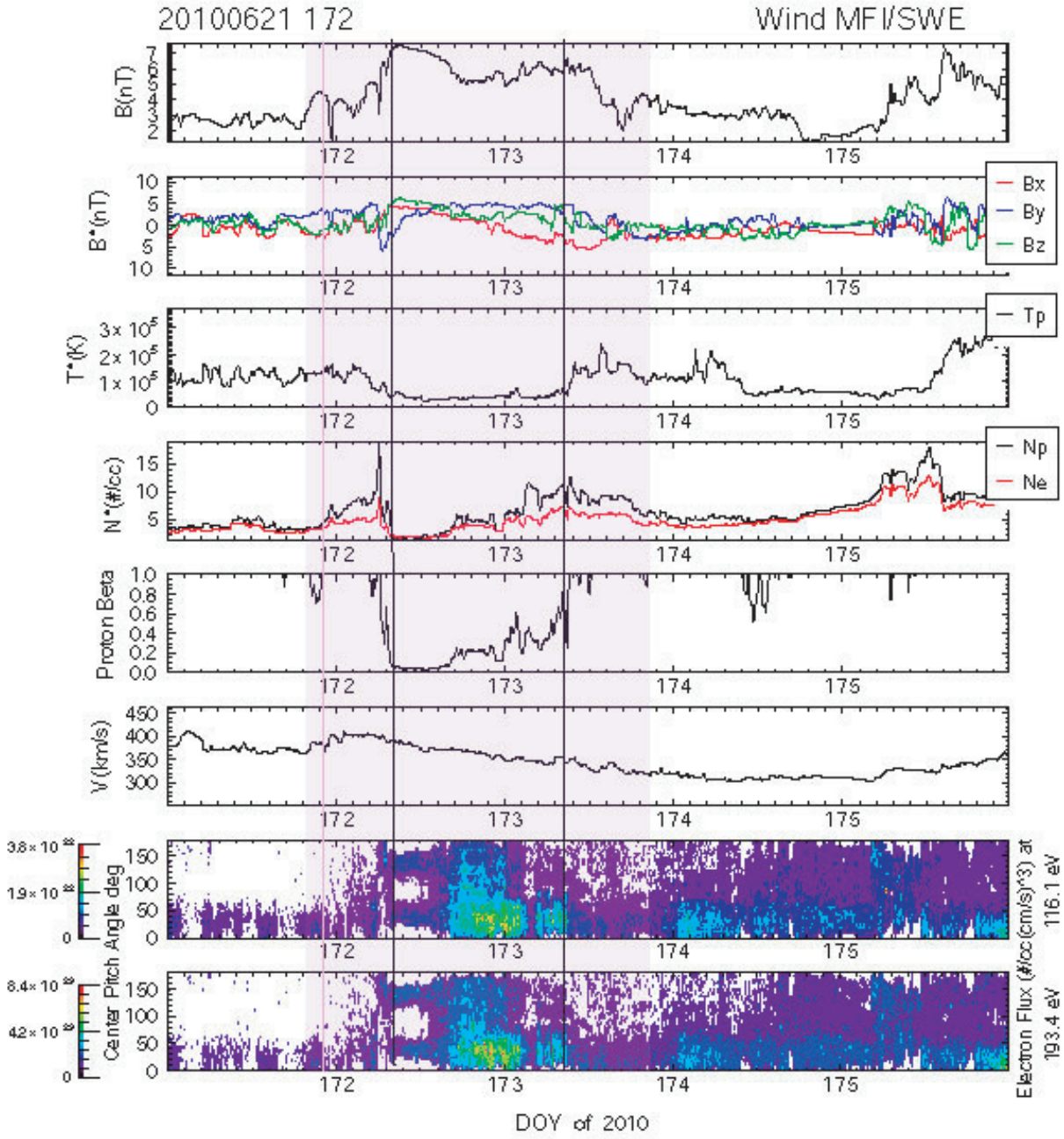

Figure 3. In-situ data from the MFI and SWE instruments onboard the Wind spacecraft. From the top, the magnetic field components and magnitude, proton plasma temperature and density, the solar wind bulk velocity. Below, the electron pitch angle distribution for different energy levels are shown. The vertical black lines mark the interval of the MC.

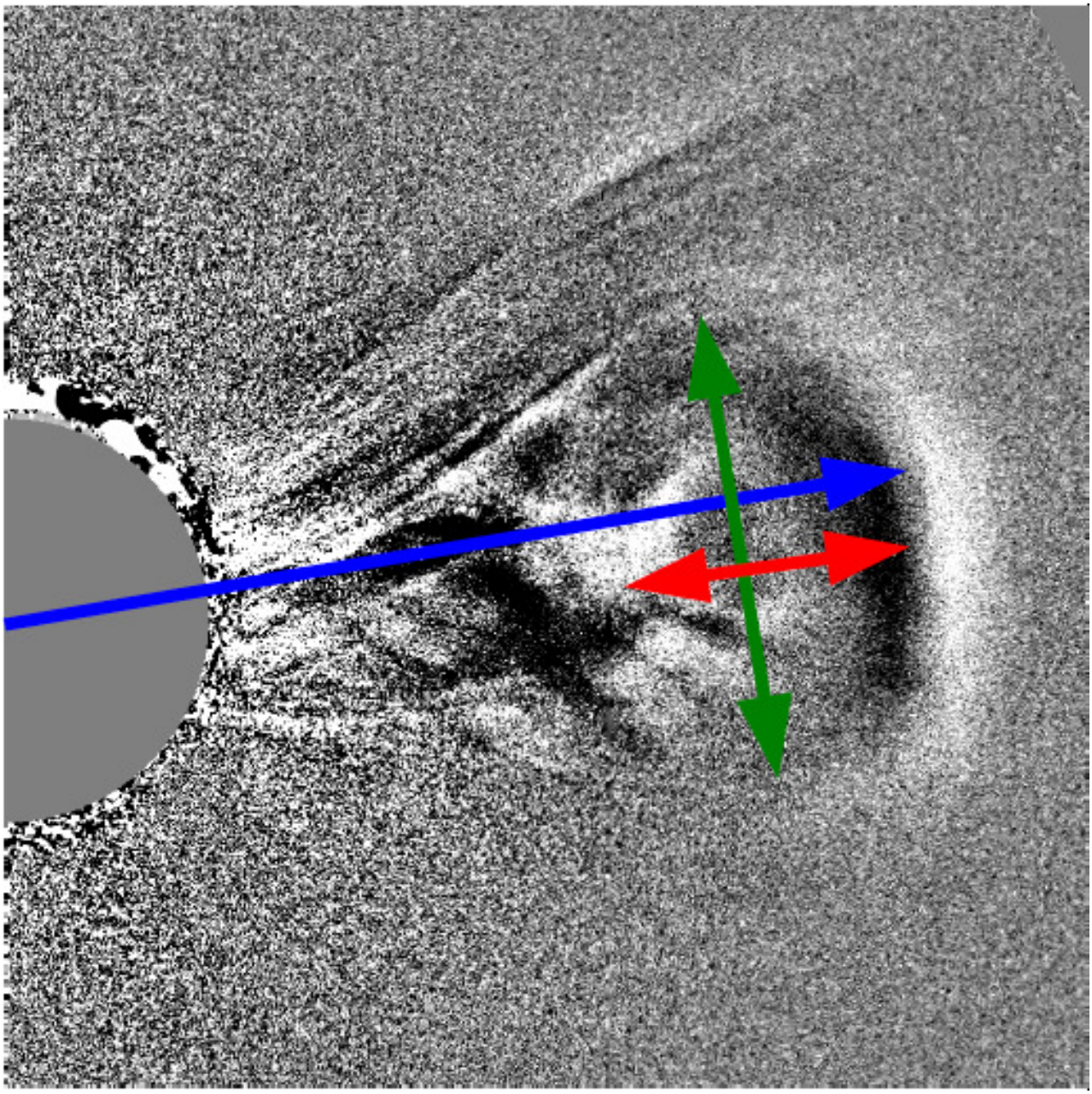

Figure 4. Image taken by STEREO A COR2 of the studied CME over-plotted with a schematic representation of the three direct measurements we made: blue -elongation; red - parallel CME cross-section diameter; and green - perpendicular CME cross-section diameter.

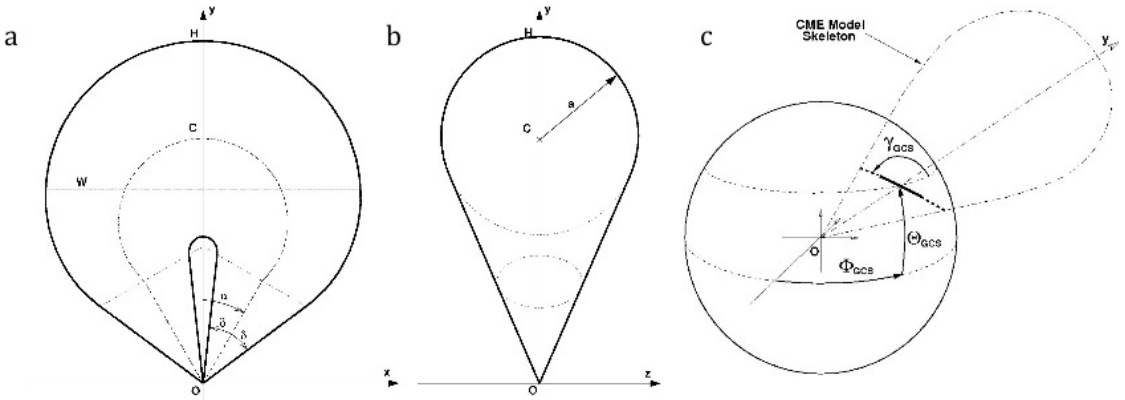

Figure 5. Representation of the graduated cylindrical shell (GCS) model (a) face-on, (b) edge on, and (c) the 3D representation. The dash-dotted line is the axis through the center of the shell. The solid line represents a planar cut through the cylindrical shell at the origin. The width (W) of the model is defined as the largest vertical extent, dotted line. The radius, a, defines the circular cross-section. These values are controlled by the model fitting parameters: height (H), the Carrington longitude (ϕ_{GCS}), heliographic latitude (θ_{GCS}), and the tilt angle (γ_{GCS}) [Thernisien et al., 2009].

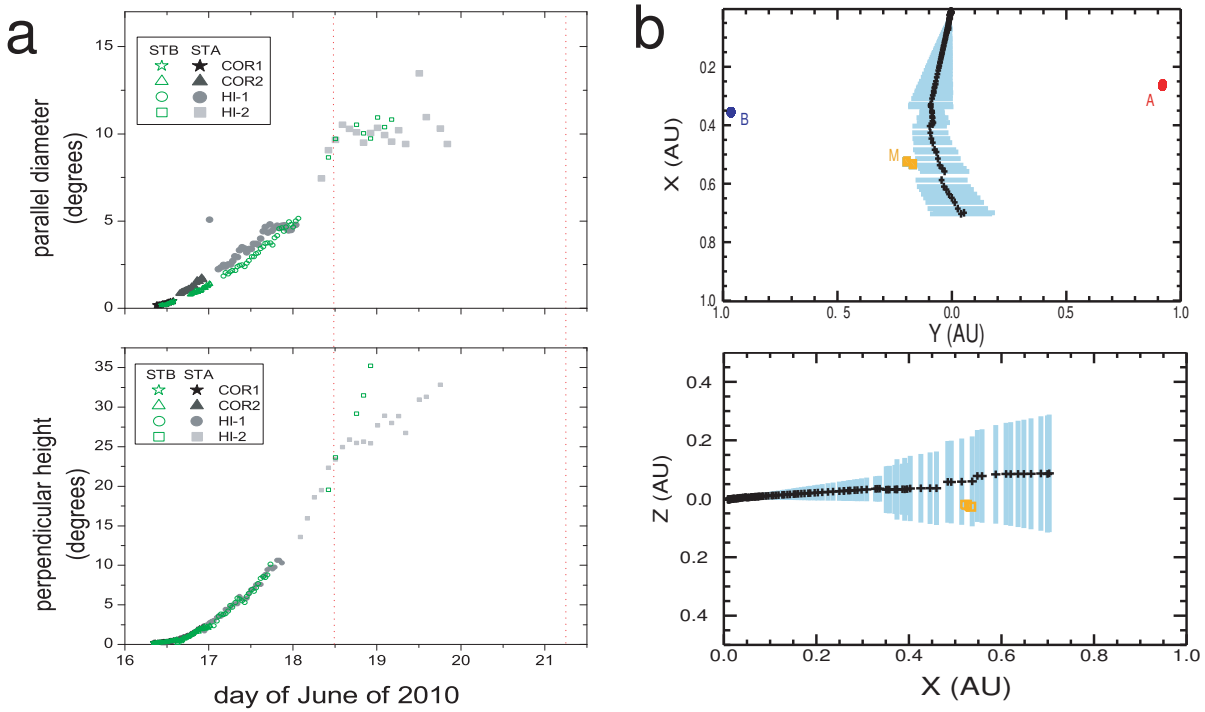

Figure 6. a) Shows the parallel (top) and perpendicular (bottom) diameters obtained from height-time measurement of the data from the STEREO A and B SECCHI sets of instruments. The dotted vertical lines mark when the in situ spacecraft detected the front of the ICME. b) Shows the results of the CGS model fitting of the CME. On the top, the sequence projected onto the ecliptic plane. The plus signs indicate the apex of the model and the blue lines provide the projected extent of the model fit. The positions of the STEREO A and B spacecraft and MESSENGER spacecraft are shown by red, blue and orange dots, respectively. On the bottom, the sequence projected onto the Sun-Earth plane. Orange dot is the MESSENGER spacecraft position and Earth is at the (1,0,0) position.

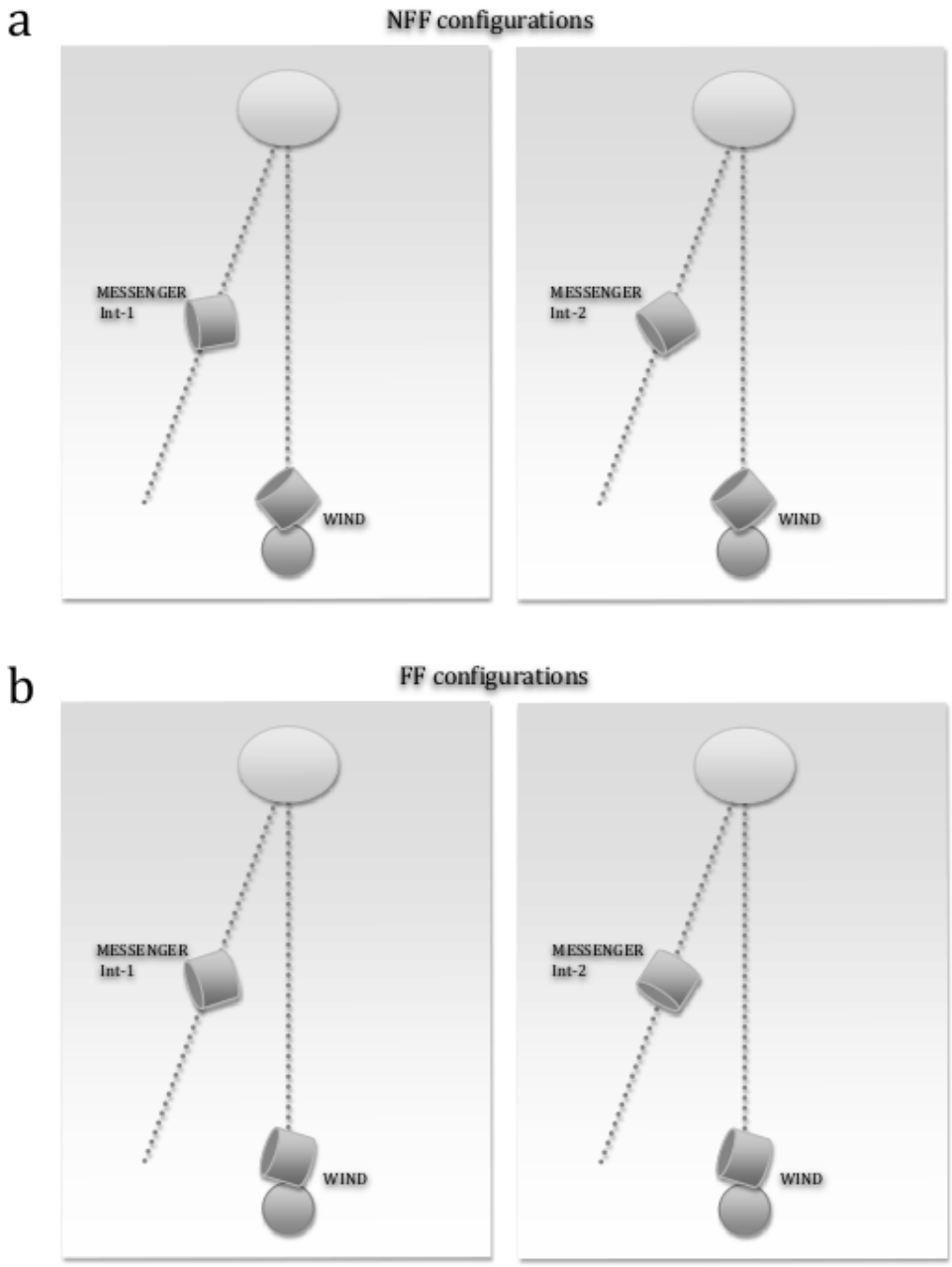

Figure 7. The possible configurations on the ecliptic plane for the MC evolution as predicted by the in situ analytical models a) FF= Force Free, and b) NFF = Non Force Free. The detailed values are in the Table 2.

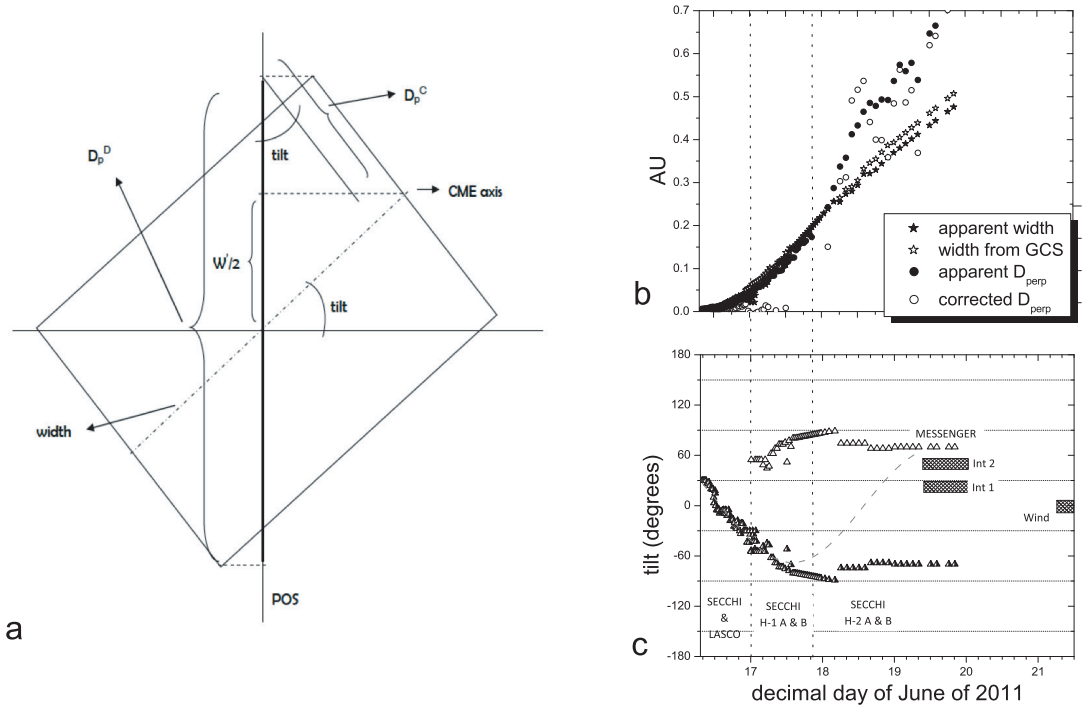

Figure 8. a) Correction, due to the CME/ICME rotation, to the projected perpendicular diameter measurements using the tilt and width (W) obtained from the GCS model. b) Shows perpendicular direct measurements of remote sensing data, the same data corrected due CME/ICME rotation and the width obtained by GCS technique and the projection onto the POS. c)The tilt of the CME from the low solar corona up to 1 AU. Filled triangles represent the values obtained with CSG technique. White triangles represent the symmetric tilt projection in the POS. The values obtained with the NFF in-situ model are shown by the two cross-hatched rectangles at 0.5 AU (two probable time intervals) and other at 1 AU. Vertical dash lines delimit the FOV detectors.

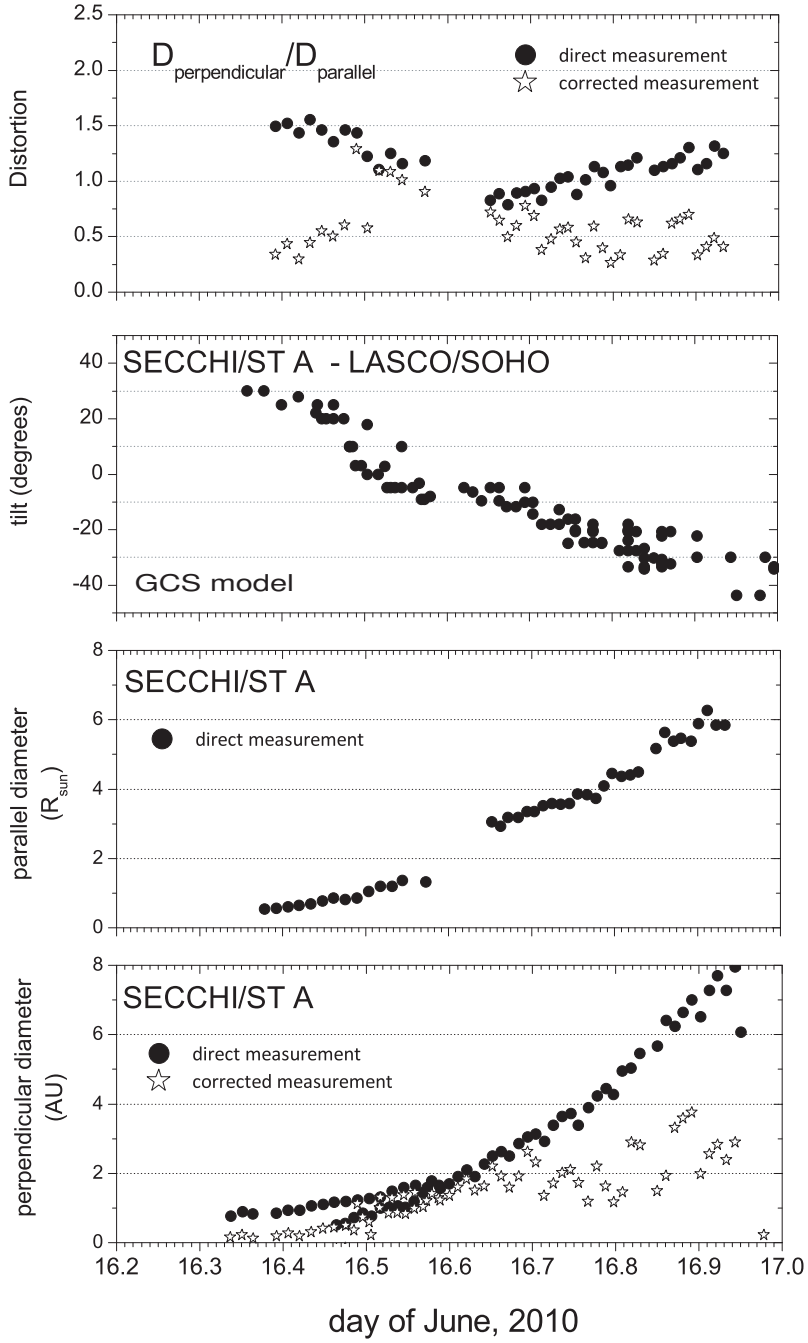

Figure 9. Combined analysis of the expansion and distortion of the CME/ICME for the period of time when LASCO/SOHO and SECCHI/STEREO spacecraft observed the event simultaneously. The best results from the GCS model are obtained when the CME is observed from all three viewpoints. From the bottom, the perpendicular direct (dots) and corrected measurement (stars), parallel diameter, tilt, and the distortion obtained from the direct and corrected data measurement are shown.

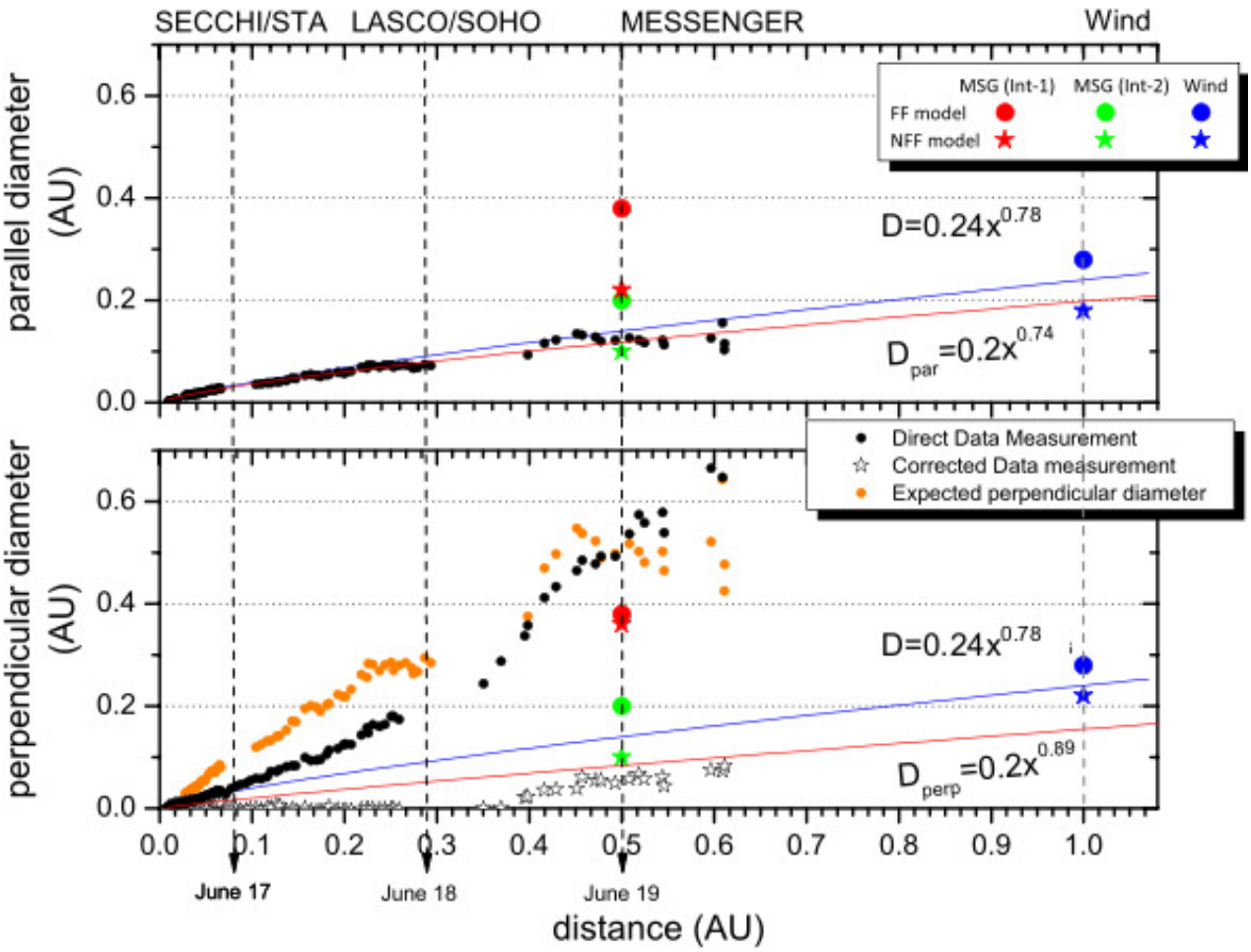

Figure 10. Combined analysis of the expansion of the parallel (top) and perpendicular (bottom) diameters of the ICME/CME cross section over 1 AU. The perpendicular diameters are corrected. Black dots represent the direct data measurements taken from the SECCHI/STEREO A images. Green and red dots/stars represent the results obtained with the in-situ analytical model at 0.5 and 1 AU. The blue lines are the empirically derived expansion assuming a circular cross section [Bothmer & Schwenn, 1998]. The red line represents the fit to the deprojected perpendicular data from Sun to 0.3 AU. Orange dots are the expected perpendicular diameters from Savani et al. [2011].

Table 1. The table on the top shows the observations by STEREO A and B: first time observation by each SECCHI detector (COR1, COR2, HI1 and HI2), the FOV (field of view) cover by detector, mean velocity and PA (pitch angle) measured in the interval. On the bottom table, from the in-situ observations of MESSENGER at 0.5 AU and Wind at 1 AU, the front and rear time for the MC boundaries, the mean velocity and the higher magnetic field detected by the magnetometer onboard each spacecraft.

REMOTE OBSERVATIONS

Spacecraft	FOV ($R_\odot$)	T_{start} UT	V_{mean} (km/s)	PA (^{0})
STEREO A/SECCHI				
COR1	1.4 - 4.0	Jun 16 06:05	64	96
COR2	2.5 - 15	Jun 16 11:08	206	88
HI1	15 - 86	Jun 16 22:06	389	87
HI2	68 - 318	Jun 18 02:09	299	89
STEREO B/SECCHI				
COR1	1.4 - 4.0	Jun 16 06:05	62	270
COR2	2.5 - 15	Jun 16 15:08	224	278
HI1	15 - 86	Jun 16 22:49	395	276
HI2	68 - 318	Jun 18 04:09	374	277
SOHO/LASCO				
C2	2.5 - 6.0	Jun 16 14:54	123	79
C3	4.0 - 30	Jun 16 19:42	294	62

IN-SITU OBSERVATIONS

Spacecraft	Position		T_{start}	T_{end}	V_{sw}	B_{max}
MESSENGER	0.5 AU	Int-1$^{(**)}$	06/19/10 10:48:00	06/20/10 2:24:00	350 km/s$^{(*)}$	31 nT
MESSENGER	0.5 AU	Int-2$^{(**)}$	06/19/10 3:45:00			
Wind	1 AU		06/21/10 7:12:00	06/22/10 7:12:00	365 km/s	8.6 nT

$^{(*)}V_{sw}$ is the estimated solar wind bulk velocity using the first time remote observation and the time arrival to Wind.

$^{(**)}$ Two possible start times for flux rope observed by MESSENGER.

Table 2. Parameters obtained with in-situ force-free (FF) circular model and non force-free (NFF) elliptical model. Two intervals have been chosen for MESSENGER data, table 1.

S/P	j_η μA/km^2	j_y^0 μA/km^2	B_y^0 nT	ϵ (%)	ϕ^{model} (°)	$tilt^{model}$ (°)	ξ (°)	y_0 AU	R_{max} AU	ϕ_t 10^{20}Mx	j_0 μA/km^2	*corr*
MESS	Int-1											
NFF	0.45	0.35	43.86	55	120	38	158	0.067	0.180	60.2	0.5	0.52
FF			27.10		128	10		0.034	0.151	19.0	2.3	
MESS	Int-2											
NFF	1.92	3.66	29.00	96	144	43	159	0.017	0.049	4.7	8.02	0.64
FF			25.11		167	69		0.017	0.092	6.6	3.5	
Wind												
NFF	0.19	0.86	9.7	86	41	-14	174	0.046	0.104	6.8	0.68	0.86
FF			9.60		73	6		0.085	0.134	6.1	0.85	